Volume 18
Number 13
7 July 2025
Pages 6311–6842

Energy & Environmental Science

rsc.li/ees

ISSN 1754-5706

ROYAL SOCIETY
OF **CHEMISTRY**

PAPER
Mingxian Liu *et al.*
High-conversion-efficiency and stable six-electron $Zn-I_2$ batteries enabled by organic iodide/thiazole-linked covalent organic frameworks

Energy &
Environmental
Science

ROYAL SOCIETY
OF CHEMISTRY

PAPER

View Article Online
View Journal | View Issue

Check for updates

Cite this: *Energy Environ. Sci.*, 2025, **18**, 6540

Received 20th January 2025,
Accepted 8th April 2025

DOI: 10.1039/d5ee00365b

rsc.li/ees

High-conversion-efficiency and stable six-electron Zn–I_2 batteries enabled by organic iodide/thiazole-linked covalent organic frameworks†

Wenyan Du,[a] Qi Huang,[b] Xunwen Zheng,[a] Yaokang Lv,[d] Ling Miao,[a] Ziyang Song,[a] Lihua Gan[ac] and Mingxian Liu*[ac]

Six-electron I^-/I^{5+} redox chemistry gives a promising platform to achieve high-capacity Zn–I_2 batteries, but faces limited conversion efficiency and instability of IO_3^- species. Here, we design a thiazole-linked covalent organic framework (TZ-COF) hosted organic trimethylsulfonium iodide (C_3H_9IS/TZ-COFs) electrode in a 1-methyl-3-propylimidazolium bromide (MPIBr)-containing electrolyte to stimulate $I^-/I^0/I^+/I^{5+}$ iodine conversion chemistry with better electrochemical efficiency and stability. Compared with inorganic symmetric I_2 molecules, the more easily exposed I^- center of polar C_3H_9IS combines with the oxygen in H_2O to form HIO_3, which initiates 6e$^-$ I^-/IO_3^- conversion through I^+ activation of MPIBr, thus reducing the oxidation/reduction potential gap to achieve 97% iodine conversion efficiency. Meanwhile, thiazole units of TZ-COFs enable strong chemical adsorption with IO_3^- species to improve redox stability with high reversibility due to reduced energy barriers (−5.1 *vs.* −3.5 eV in activated carbon (AC) host) and upgraded conversion kinetics (activation energy: 0.21 *vs.* 0.38 eV in AC). Such a stable and high-efficiency 6e$^-$ iodine conversion gives C_3H_9IS/TZ-COFs electrodes record high capacity (1296 mA h g^{-1}) and energy density (1464 W h kg^{-1}), and superior cycling stability (1200 cycles). These findings constitute a major advance in the design of iodine redox chemistry towards state-of-the-art Zn–I_2 batteries.

Broader context

Recently, 6e$^-$ iodine conversion (I^-/IO_3^-) chemistry has been achieved *via* hetero-halogen chemistry activation, which boosts iodine conversion kinetics and reversibility to achieve Zn–I_2 batteries with high capacity and energy density. Nevertheless, the electrochemical formation of hypervalent iodine (I^{5+}) is impeded by low conversion efficiency and unstable intermediates, limiting further exploration of multi-electron iodine electrochemistry in the realm of energy storage. In this work, we design a thiazole-linked covalent organic framework (TZ-COF) hosted organic trimethylsulfonium iodide (C_3H_9IS/TZ-COFs) electrode in a 1-methyl-3-propylimidazolium bromide (MPIBr)-containing electrolyte to stimulate $I^-/I^0/I^+/I^{5+}$ iodine conversion chemistry with better electrochemical efficiency and stability. The high iodine conversion efficiency (97%) and stable 6e$^-$ iodine conversion bring the capacity and energy density of Zn–I_2 batteries to a new level. This work broadens the horizons of multielectron redox chemistry for building advanced Zn–I_2 batteries.

Introduction

Rechargeable zinc–iodine batteries have garnered significant attention due to environmental friendliness, high abundance, and diversity in the valence of iodine.[1–6] However, a traditional iodine electrode operates as a one-electron transfer I^-/I_2 redox couple, exhibiting a relatively low theoretical capacity (211 mA h g^{-1}), a low discharge plateau (0.54 V *vs.* standard hydrogen potential), and consequently insufficient energy density.[7–13] To overcome these limitations, activating the 2 e$^-$ I^-/I^+ redox couple at high discharge voltage *via* the halogen reaction between I^- species and halides (*e.g.*, Br^-, Cl^-) has been widely reported for achieving better Zn–I_2 batteries.[14–16] Recently, the Liang group reported a 6e$^-$ iodine conversion (I^-/IO_3^-) enabled by interhalogen chemistry between I^- and Br^- ($I^- + Br^- \rightarrow I^+Br^- + 2e^-$), which offers an electrochemical–chemical loop that boosts the kinetics and reversibility of the iodine conversion reaction, facilitating a high capacity of 1200 mA h g^{-1} (80.9% iodine conversion efficiency when deducting the capacity contribution of the activated carbon

---

[a] *Shanghai Key Lab of Chemical Assessment and Sustainability, School of Chemical Science and Engineering, Tongji University, Shanghai1239 Siping Rd., 200092, P. R. China. E-mail: liumx@tongji.edu.cn*
[b] *Institute for Electric Light Sources, School of Information Science and Technology, Fudan University, 2005 Songhu Rd., Shanghai 200438, P. R. China*
[c] *State Key Laboratory of Cardiovascular Diseases and Medical Innovation Center, Shanghai East Hospital, School of Medicine, Tongji University, 150 Jimo Rd., Shanghai 200120, P. R. China*
[d] *College of Chemical Engineering, Zhejiang University of Technology, 18 Chaowang Rd, Hangzhou 310014, P. R. China*

† Electronic supplementary information (ESI) available. See DOI: **https://doi.org/10.1039/d5ee00365b**

(AC) host) and an energy density of 1357 W h kg^{-1}.[17] The Li group activated the 6e$^-$ I$^-$/IO$_3^-$ redox process using highly concentrated hetero-halogen (I$^-$ and Br$^-$) electrolytes to achieve a high capacity of 840 A h L$_{\text{catholyte}}^{-1}$ (945 mA h g^{-1}, 74.6% iodine conversion efficiency) and energy density of 1200 W h L$_{\text{catholyte}}^{-1}$ (1350 W h kg^{-1}).[18] Nevertheless, the electrochemical formation of hypervalent iodine (I^{5+}) is impeded by low conversion efficiency and unstable intermediates, limiting further exploration of multi-electron iodine electrochemistry in the realm of energy storage. Highly soluble IO$_3^-$ species are difficult to be stabilized by a common carbon host due to weak physical adsorption.[19–22] More importantly, a high energy barrier (6.01 eV), caused by a huge potential gap of 0.66 V between the I$^-$/I^0 couple (0.54 V) and I^0/I^{5+} couple (1.20 V), hinders the reversible electrochemical redox reaction from I$^-$ to IO$_3^-$, leading to slow reaction kinetics and limited conversion efficiency.[23–30] These two issues bring challenges in establishing efficient iodine redox chemistry with more electron transfer for building better aqueous Zn–I$_2$ batteries.[31–38]

In this work, we report high-conversion-efficiency and stable 6e$^-$ Zn–I$_2$ batteries enabled by organic iodide/thiazole-linked covalent organic frameworks (C$_3$H$_9$IS/TZ-COFs). The C$_3$H$_9$IS/TZ-COFs electrode in a 1-methyl-3-propylimidazolium bromide (MPIBr)-containing electrolyte stimulates I$^-$/I^0/I$^+$/I^{5+} iodine conversion with superior electrochemical efficiency and stability. Compared with conventional I$_2$, C$_3$H$_9$IS with a polar iodide center is more likely to combine with the oxygen in H$_2$O to form IO$_3^-$ species, initiating 6e$^-$ I$^-$/I^0/I$^+$/I^{5+} iodine conversion chemistry through I$^+$ activation of MPIBr, thereby reducing the potential gap between oxidation and reduction and improving the electrochemical efficiency. Moreover, C═N/C–S motifs of thiazole units in TZ-COFs coordinate with IO$_3^-$ solving the solubility and stability issues, and simultaneously catalyze reversible iodine conversion from I$^-$ to IO$_3^-$ due to the reduced energy barriers and the boosted redox reaction kinetics. The high iodine conversion efficiency (97%) and stable 6e$^-$ iodine conversion bring the capacity and energy density of C$_3$H$_9$IS/TZ-COFs electrodes to a new level. This work broadens the horizons of multielectron redox chemistry for building advanced Zn–I$_2$ batteries.

Results and discussion

Naphthalene-2,6-diamine (ND), benzene-1,3,5-tricarbaldehyde (TA) and sulfur can undergo an oxidative annulation reaction to form highly crystalline TZ-COFs under solvothermal conditions (Fig. 1a).[39] Powder X-ray diffraction (PXRD) patterns of TZ-COFs exhibit typical diffraction peaks at 3.41° and 6.85° belonging to the (110) and (200) planes (Fig. 1b), confirming a highly crystalline structure. Fourier transformed infrared (FT–IR) spectra show new peaks of C═N groups at 1609 cm^{-1} and C–S groups at 673 cm^{-1} (Fig. 1c), indicating the formation of TZ-COFs. TZ-COFs are highly stable in boiling H$_2$O, 12 M HCl or KOH solution for 24 h, suggesting excellent acid–alkali resistance and thermal stability (Fig. 1b, c and Fig. S1, ESI†). Scanning electron microscopy (SEM) and transmission electron microscopy (TEM) images reveal the rod-like geometry of TZ-COFs with a lattice space of 0.3 nm (Fig. 1d and e). C═N/C–S motifs of thiazole units in TZ-COFs show negative molecular electrostatic potential (MEP),[40] and are the desirable active sites (blue area) to anchor iodine species (Fig. 1f and Fig. S2, ESI†), while the remaining domains (red area) around the aromatic ring maintain electron localization. Besides, TZ-COFs have a low optical energy gap (E_g) of 2.01 eV (Fig. 1g), which affords desirable electron conductivity and swift charge transport for stimulating high-kinetics redox reactions. The localized orbital locator-π (LOL-π) color-filled map[41] unravels the connected isosurfaces of TZ-COFs, validating the highly conjugated organic structure and the electron delocalization effect (Fig. 1h).

Due to the exposed polar iodide center and high stability, C$_3$H$_9$IS is elaborately selected as the iodine source, which includes the C$_3$H$_9$S$^+$ chain and the I$^-$ anion connected by a weak ionic bond (Fig. S3, ESI†). To solve the problems of inevitable dissolution in aqueous electrolytes and low conductivity, C$_3$H$_9$IS was encapsulated in porous TZ-COFs (Fig. S4, ESI†) *via* the fusion-diffusion method to obtain the C$_3$H$_9$IS/TZ-COFs electrode. The electrochemical performances of the C$_3$H$_9$IS/TZ-COFs electrode were studied using a three-electrode Swagelok cell with a Ti mesh as the counter electrode and Hg/HgCl$_2$ as the reference electrode in an aqueous Zn(OTF)$_2$-MPIBr electrolyte (Fig. S5, ESI†).

Galvanostatic charge–discharge (GCD) curves of the C$_3$H$_9$IS/TZ-COFs electrode show an ultrahigh capacity of 1296 mA h g^{-1} (Fig. 2a), which exceeds those of C$_3$H$_9$IS/N-COFs (1202 mA h g^{-1}), C$_3$H$_9$IS/activated carbon (AC) (1023 mA h g^{-1}), and TZ-COFs (34 mA h g^{-1}) electrodes (Fig. 2b and Fig. S6, S7, ESI†). A small voltage polarization of 0.28 V enabling 97% iodine conversion efficiency can be observed in the GCD curves of the C$_3$H$_9$IS/TZ-COFs electrode, indicating a fast reduction/oxidation kinetics process. With the increase of current density from 1 to 5 A g^{-1}, the C$_3$H$_9$IS/TZ-COFs electrode still holds a high capacity of 762 mA h g^{-1}, suggesting the inhibition of the iodine species shuttle and improved conversion kinetics during (dis)charging. The high capacity and average discharge voltage endow the C$_3$H$_9$IS/TZ-COFs electrode with a record high energy density of 1464 W h kg^{-1} (based on the mass loading of C$_3$H$_9$IS in the electrode, Fig. 2c),[7,8,14,15,17,18,26,42–48] rendering it the state-of-the-art Zn–I$_2$ battery electrode (Table S1, ESI†). Significantly, the C$_3$H$_9$IS/TZ-COFs electrode delivers a high-capacity retention of 83.6% over 1200 cycles (Fig. 2d), outperforming C$_3$H$_9$IS/N-COFs (30% over 540 cycles) and C$_3$H$_9$IS/AC electrodes (10% over 420 cycles). Compared with soluble C$_3$H$_9$IS/N-COFs and C$_3$H$_9$IS/AC electrodes, the C$_3$H$_9$IS/TZ-COFs electrode prevents the iodine shuttle and thus promotes iodine conversion for activating better capacity storage. Furthermore, the electrochemical impedance spectra after cycling also display a small diffusion resistance (R_{ct}) for the C$_3$H$_9$IS/TZ-COFs electrode (Fig. S8, ESI†), implying rapid redox kinetics of iodine species in TZ-COFs.

The charge storage kinetics of the C$_3$H$_9$IS/TZ-COFs electrode was further studied by Dunn's method.[49–53] Cyclic voltammetry (CV) profiles distinctly exhibit three pairs of redox signals (denoted as P_{R1}, P_{R2}, P_{R3}, P_{O1}, P_{O2} and P_{O3}, Fig. 2e), indicative of a multi-step electrochemistry. The peak shape is almost the same with the

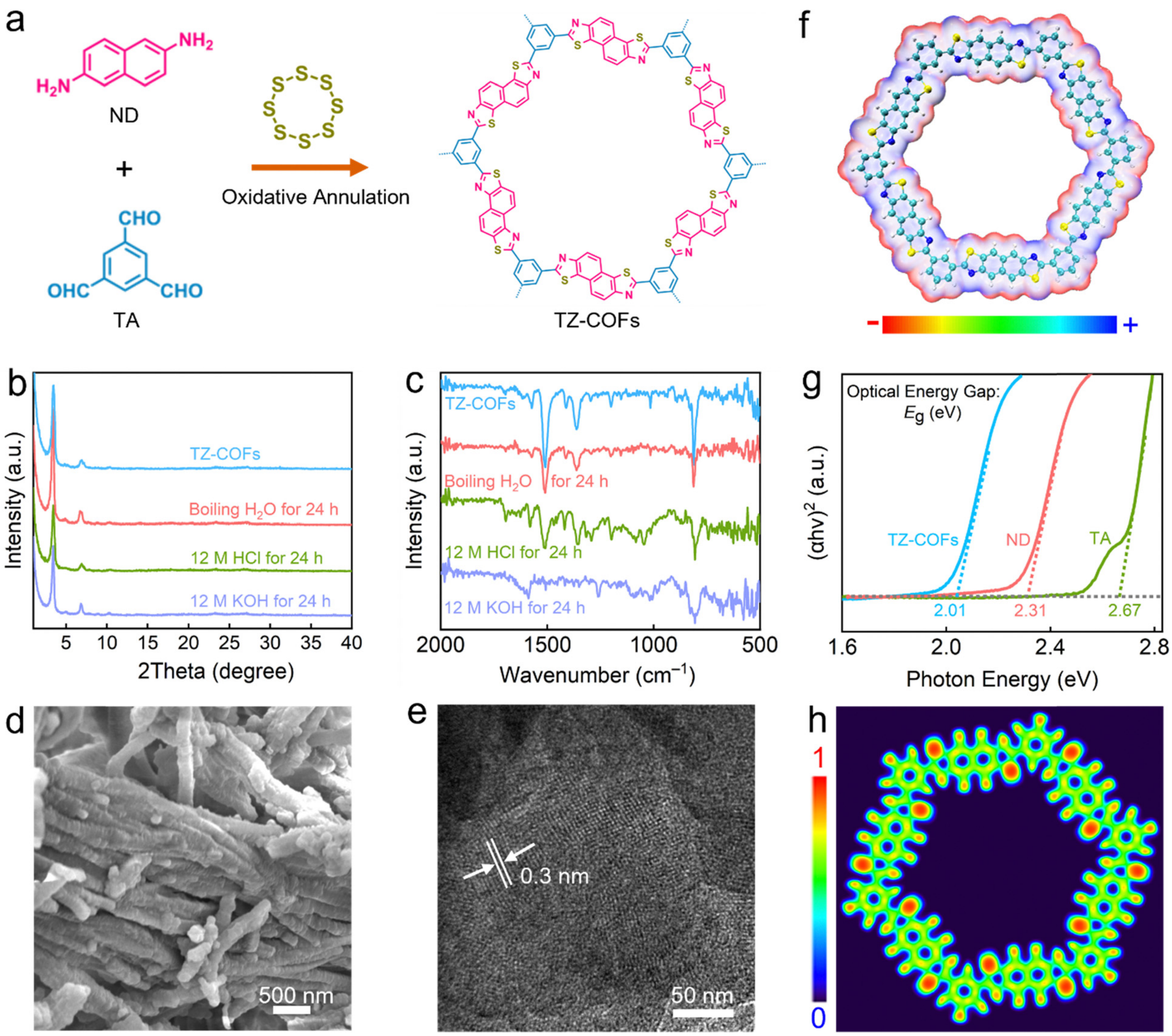

Fig. 1 Structural characterization of TZ-COFs. (a) Synthesis process of TZ-COFs. (b) XRD patterns. (c) FT-IR spectra. (d) SEM and (e) TEM images. (b) Optimized molecular structures and energy levels. (f) ESP simulation. (e) E_g values. (h) LOL-π map.

increase of the scan rate from 0.1 to 0.5 mV s^{-1}, substantiating the superb electrochemical reversibility and ion diffusion kinetics. The relationship between current (i) and scan rate (v) can be expressed as $i = kv^b$, where k is constant.[54–56] Plotting $\log(i)$ against $\log(v)$ yields high power-exponent b values of 0.92–0.84 for the eight redox peaks (Fig. S10, ESI†), signifying the fast surface-controlled charge-storage kinetics. Almost 95% of the total stored charge is contributed by the surface redox reaction at 0.5 mV s^{-1} (Fig. S11, ESI†), along with the slight diffusion-limited process (5%). With incremental scan rate, the capacitive contribution dominates the diffusion-limited contribution, and gradually increases from 83 to 95% (Fig. 2f). This contributes to the surface-dominated capacitive charge storage for fast charge carrier transport in the TZ-COFs/C_3H_9IS electrode, which well explains its superior high-rate capability as reflected in the GCD curves (Fig. 2a).

To verify the redox mechanism of the C_3H_9IS/TZ-COFs electrode in the $Zn(OTF)_2$-MPIBr electrolyte, *ex situ* Raman spectra were performed to reveal its structural evolution at different voltage states (Fig. 3a and b).[18,57,58] At the initial state, a signal at 110 cm^{-1}, the vibrational peak of $C_3H_9S{-}I$, corresponds to I^-, which confirms the presence of C_3H_9IS in TZ-COFs. Upon increasing the voltage to 0.54 V, a new peak is identified at 182 cm^{-1} ascribed to I_2,[1,18,46] indicating the progress of the first redox stage for I^-/I_2 (corresponding to 0.54/0.41 V in CV profiles). When I^- ions are oxidized into iodine at the electrode, it spontaneously reacts with I^- forming I_3^- species ($2I^- - 2e^- \rightarrow I_2$, $I_2 + I^- \rightarrow I_3^-$). Given the fact that I_3^- cannot be effectively distinguished by the Raman spectrum because it is roughly at the same position as the I^- peak, we further confirm the generated I^- through the UV-vis spectra (325 nm for I_3^-, Fig. 3c). As the voltage increases to 0.93 V, a distinctive peak appears at 214 cm^{-1}, which is associated with the formation of IBr species, suggesting the I_2/IBr redox reaction.[17] During charging to 1.20 V, two new signals emerge at 310/320 cm^{-1} and 780 cm^{-1} ascribed to IO_3^- species, confirming the I^+ to IO_3^- conversion.[18,59,60] Overall, a multi-step multielectron redox reaction can be clarified for the

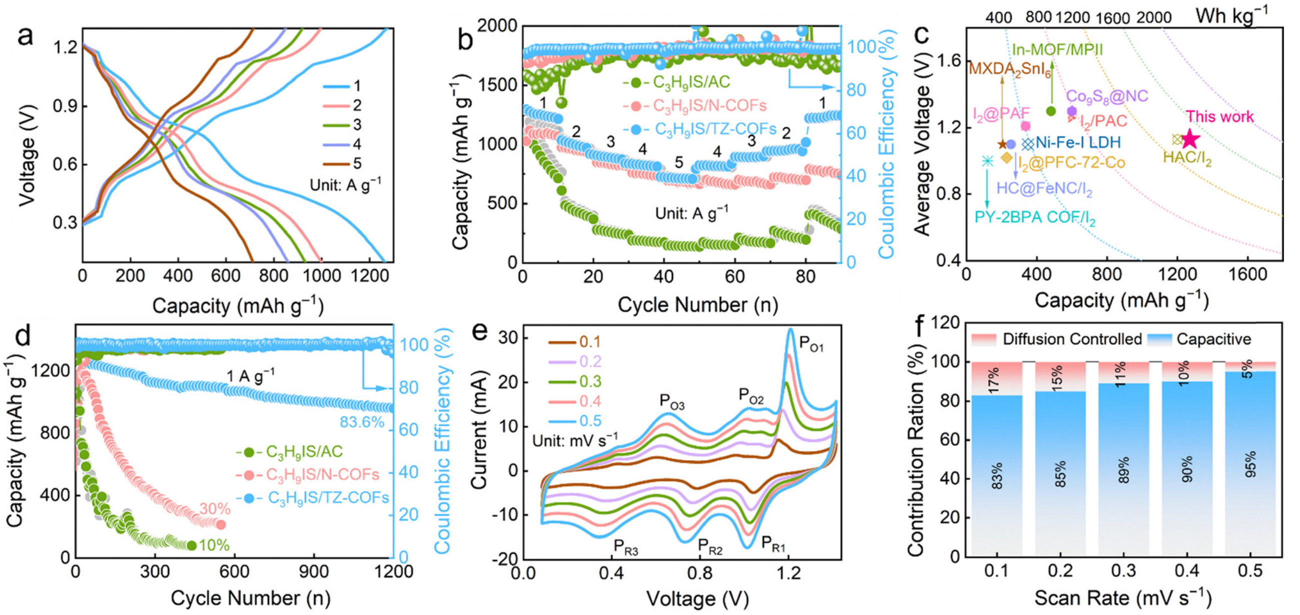

Fig. 2 Electrochemical metrics of Zn–I_2 batteries. (a) GCD curves. (b) Rate capacities. (c) Contour plots of energy density compared with reported Zn–I_2 batteries. (d) Cycling stability. (e) CV curves at various scan rates. (f) Capacitive and diffusion-controlled contribution of the C_3H_9IS/TZ-COFs electrode at various scan rates.

C_3H_9IS/TZ-COFs electrode, involving I^-/I_2 (0.54/0.41V), I_2/I^+ (0.93/0.80V) and I^+/IO_3^- (1.20/1.03 V) conversions. During subsequent discharging, all peaks return to their initial levels, suggesting the highly reversible $I^-/I^0/I^+/I^{5+}$ conversion redox chemistry. In the *ex situ* UV-vis spectra of the C_3H_9IS/TZ-COFs electrode at different states (Fig. 3c), a prominent peak at 225 nm at the initial state is observed, which corresponds to I^- from C_3H_9IS. As the voltage increases to 0.54 V, new peaks at 287/445 nm appear, indicating the presence of I_2 species.[1] As the voltage increases to 0.93 V, new peaks at 254 and 205 nm appear, indicating the presence of IBr species and the formation of IO_3^- species, respectively.[17,18] Furthermore, the charging of the cell gives rise to the formation of Br_2 which is ascribed to the oxidation of IBr interhalogen. Upon charging to 1.20 V, the signal peak of IO_3^- at 205 nm becomes stronger, while the characteristic peak of I^+ disappears, indicating I^+ to IO_3^- conversion.

The valence states of iodine species in the C_3H_9IS/TZ-COFs electrode were further evidenced by X-ray photoelectron spectroscopy (XPS) at different voltages (Fig. 3d). Two signals appearing at high binding energies of 628.4/619.6 eV at 0.54 V correspond to I_2 species. With the deepening of the charging to 0.93 V, higher binding energy peaks at 630.1/622.4 eV can be observed, which originate from the I^+ ion. Upon further charging to 1.20 V, the binding energy peaks of iodine species continuously shift, accompanied by suggesting the formation of I^{5+} ions. These results indicate a highly reversible $I^-/I_2/I^+/I^{5+}$ redox reaction, and are consistent with Raman spectral results. The changes on the surface of the C_3H_9IS/TZ-COFs electrode during charging–discharging process were also inspected using *ex situ* SEM images (Fig. S12, ESI†). During initial charging to 0.54 V, bulk I_2 particles can be observed on the electrode. Formed oil droplets upon further charging indicate the presence of IO_3^-. Upon further charging to 1.20 V, most IO_3^- droplets are converted into mist matter that covers the electrode surface. Upon discharge, the misty matter gradually disappears, and the bulk I_2 species are regenerated. *Ex situ* Raman spectra (Fig. 3a) and XPS spectra (Fig. 3d) confirm the generation of I^+ species, implying the formation of IBr intermediates ($I^- + Br^- \rightarrow I^+Br^- + 2e^-$) during multielectron I^-/IO_3^- iodine conversion.

The CV curve of the C_3H_9IS/TZ-COFs electrode based on the Zn(OTF)$_2$-MPIBr electrolyte exhibits three pairs of redox peaks at 0.54/0.41, 0.93/0.80, and 1.20/1.03 V corresponding to the I^-/I_2, I_2/I^+, and I^+/IO_3^- couples (Fig. 3e and Fig. S13, ESI†), respectively. Specifically, the C_3H_9IS/TZ-COFs electrode initiates 2 e^- conversion from I^+ to I^- to deliver a capacity of 330 mA h g^{-1} and 4 e^- IO_3^-/I^+ conversion to deliver an ultrahigh capacity of 966 mA h g^{-1} (Fig. 3f) with a discharge potential of 1.13 V of the Zn–I_2 system, exhibiting 97% iodine conversion efficiency. The self-discharge behavior of the Zn–I_2 battery is observed under the fully charged condition of 1.3 V, which shows a high-capacity retention of 93% after a rest step of 3 days, indicating good anti-dissolution and slight shuttle behavior (Fig. S14, ESI†). By contrast, three redox signals for I^- to IO_3^-conversion in the C_3H_9IS/AC electrode were observed in the first curve, but this conversion is irreversible in the second cycle, highlighting the key role of TZ-COFs in catalyzing reversible 6e^- conversion from I^- to IO_3^- (Fig. S15–S17, ESI†). The CV curve of the Zn‖I_2/TZ-COFs battery shows only a pair of redox peaks at 0.54/0.42 V (Fig. S18, ESI†), corresponding to a typical I^-/I_2 conversion reaction, which contributes a capacity of 154 mA h g^{-1} at 1 A g^{-1}.[1e, 2c, 7a] The excellent performance of the C_3H_9IS/TZ-COFs electrode highlights the key role of the C_3H_9IS/TZ-COFs electrode in the MPIBr-containing electrolyte to stimulate $I^-/I^0/I^+/I^{5+}$ iodine conversion chemistry with high electrochemical efficiency and stability (Fig. 3g and Fig. S19–S21, ESI†).

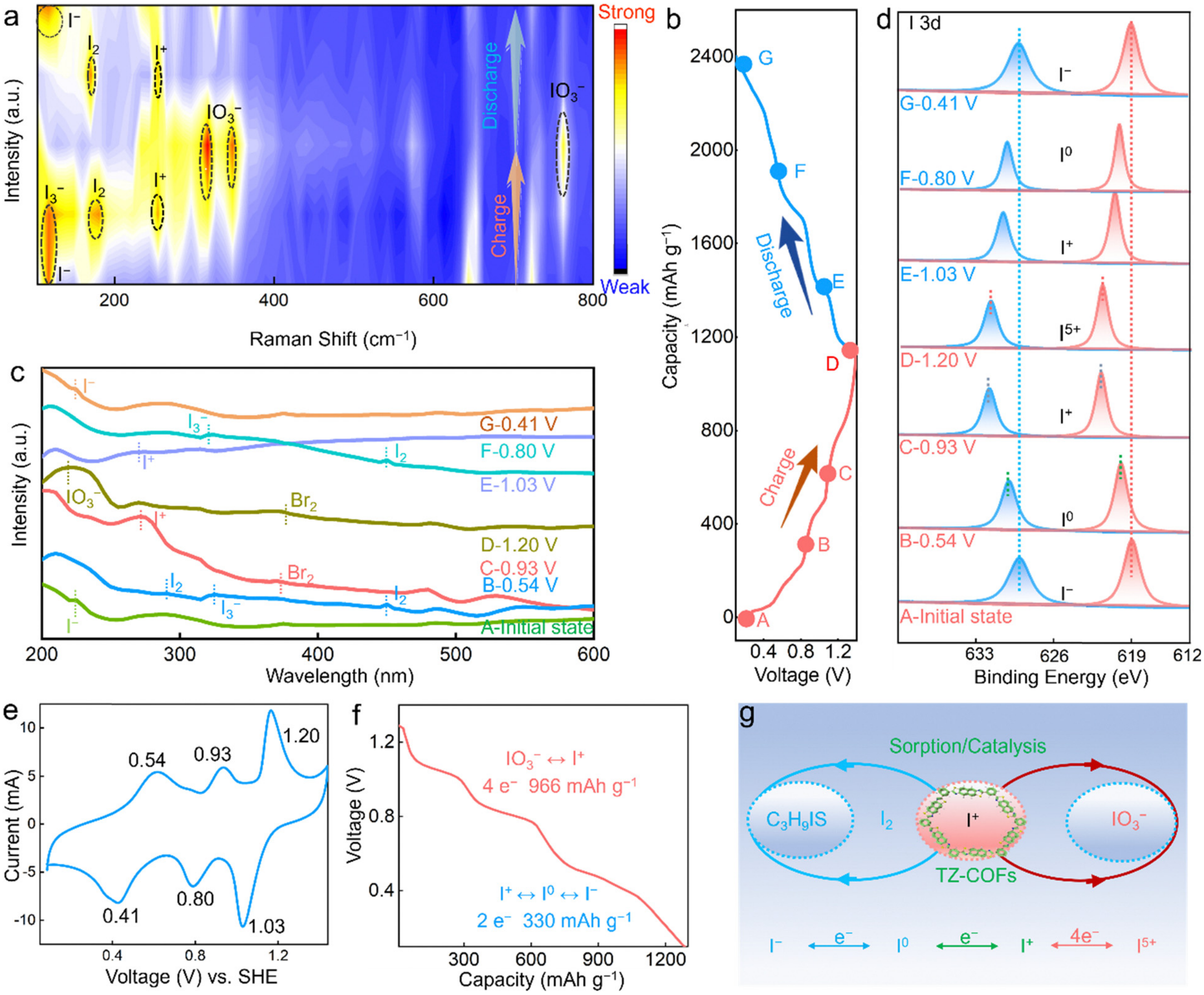

Fig. 3 Iodine redox conversion mechanism. (a) Raman spectra. (b) GCD curves. (c) UV-vis spectra. (d) High-resolution I 3d XPS spectra of the C_3H_9IS electrode at various charge/discharged states. (e) CV curve of the C_3H_9IS/TZ-COFs electrode. (f) GCD curves of the C_3H_9IS/TZ-COFs electrode at 1 A g^{-1}. (g) Iodine redox chemistry during the operation of Zn–I_2 batteries.

The binding energies of I_2 and C_3H_9IS with H_2O were calculated (Fig. S22, ESI†). C_3H_9IS/H_2O interaction (−0.81 eV) is stronger than that of I_2/H_2O (−0.42 eV). Compared with I_2, C_3H_9IS in TZ-COFs can start multielectron iodine conversion with much lower binding energy due to the more easily exposed I^- center to combine with the oxygen in H_2O to form HIO_3.[61,62] Therefore, the difference in reaction energy barriers between I_2 and C_3H_9IS is partly responsible for different redox voltages of the C_3H_9IS/TZ-COFs electrode. However, the reasons for this large difference in iodine conversion voltages are complicated and still need a further extensive and in-depth study. Overall, a highly reversible $I^-/I_2/I^+/I^{5+}$ redox reaction is triggered in the C_3H_9IS/TZ-COFs electrode (Fig. 3g), contributing to record high capacity and energy density. The whole conversion of iodine species can be expressed as follows:

$$I^- - e^- \leftrightarrow I^0 \quad 0.54\ \text{V} \qquad \text{(step 1)}$$

$$I^0 + Br^- - e^- \leftrightarrow I^+Br^- \quad 0.93\ \text{V} \qquad \text{(step 2)}$$

$$I^+ + 3H_2O - 4\ e^- \leftrightarrow IO_3^- + 6H^+ \quad 1.20\ \text{V} \quad \text{(step 3)}$$

Generally, the dissolution and shuttling issues of soluble IO_3^- species from electrodes hinder the cycling durability of Zn–I_2 batteries.[63] In this regard, C═N/C–S motifs of thiazole units in TZ-COFs are favorable for binding iodine species to relieve their loss during battery operation (Fig. S23, ESI†). TZ-COFs coordinate with IO_3^- through C═N/C–S motifs of thiazole units to ensure the redox reversibility, and catalyze a new reversible 6e^- conversion of I^- to IO_3^- to further boost capacity (Fig. S24 and S25, ESI†). Density functional theory (DFT) calculations were performed to understand in-depth the binding affinity between TZ-COFs and iodine species (Fig. 4a and b). The adsorption energies of TZ-COFs with I^-, I_2, I_3^-, I^+ and IO_3^- (from −5.59 to −0.012 eV) are lower than those of N-COFs (from −5.22 to −0.011 eV), suggesting the strong interaction between TZ-COFs and iodine species. Of note, TZ-COFs show a more negative adsorption energy with IO_3^- than N-COFs, highlighting the significant effect of thiazole units of TZ-COFs in catalyzing reversible I^-/IO_3^- conversion.

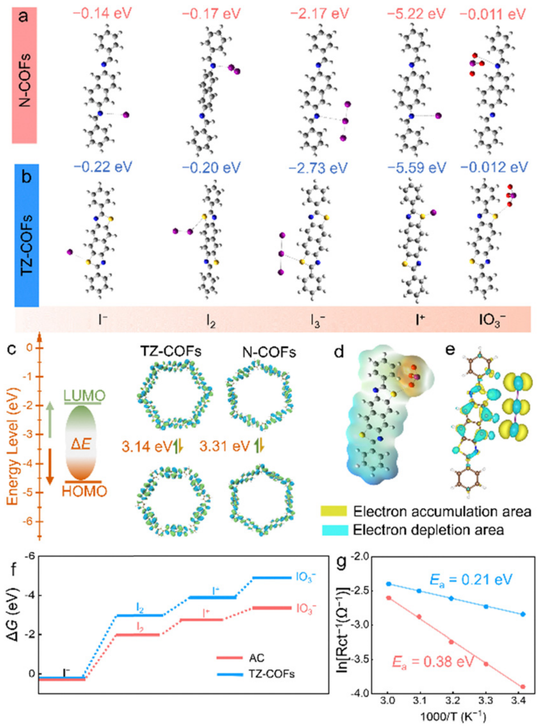

Fig. 4 Theoretical simulation of the iodine conversion process at different electrochemical states. (a) and (b) The optimized adsorption configurations of TZ-COFs and COFs. (c) HOMO and LUMO of TZ-COFs and N-COFs. (d) Interaction between the iodine species and TZ-COFs monomers. (e) The optimized charge-density-difference isosurfaces of IO_3^- adsorption on TZ-COFs. (f) Calculated cohesive energies of iodine species during TZ-COFs and AC. (g) Calculated E_a values of the C_3H_9IS/TZ-COFs electrode and the C_3H_9IS/AC electrode.

Fig. 4c shows the energy levels of the lowest unoccupied molecular orbital (LUMO) and the highest occupied molecular orbital (HOMO) for TZ-COFs and N-COFs.[40,64–66] N-COFs (only containing C═N groups) with structures similar to TZ-COFs involving C═N/C–S groups were designed as an example for comparison to study the role of catalytic sites. The energy gap (ΔE) of TZ-COFs is calculated to be 3.14 eV (Fig. 4c), which is lower than that of N-COFs (3.31 eV). It indicates that synergistic C═N/C–S sites are more favorable for boosting iodine conversion with low energy barriers. Consequently, the C_3H_9IS/TZ-COFs electrode delivers higher conversion efficiency/cycling stability (97%/1200 cycles, Fig. 2d) than C_3H_9IS/N-COFs (94%/540 cycles). Furthermore, MEP simulation and charge density difference isosurfaces suggest a strong chemical interaction between TZ-COF and IO_3^- (Fig. 4d and e), accompanied by electron accumulation (green area) and depletion (yellow area) to form a stable configuration for triggering improved electrochemical activity and durability.

The role of TZ-COFs in activating and stabilizing the 6e⁻ transfer redox reaction from I^- to IO_3^- can be further understood from DFT calculations.[67,68] The Gibbs free energy (ΔG) values of iodine species in TZ-COFs at various electrochemical states are negative than that of AC (Fig. 4f), suggesting an energy-favorable 6e⁻ $I^-/I_2/I^+/IO_3^-$ redox conversion with low energy barriers. Of note, TZ-COFs catalyze a reversible 6e⁻ conversion from I^- to IO_3^- due to reduced energy barriers (−5.1 *vs.* −3.5 eV in the AC host). Besides, the activation energy (E_a) is 0.21 eV for the C_3H_9IS/TZ-COFs electrode (Fig. 4g and Fig. S26, S27, ESI†) based on the Arrhenius equation, which is much lower than that of the C_3H_9IS/AC electrode (0.38 eV). TZ-COFs activate high-kinetics interfacial charge mobility and redox reactions to catalyze a highly reversible $I^-/I_2/I^+/IO_3^-$ conversion reaction.

Overall, the C_3H_9IS/TZ-COFs electrode in the $Zn(OTF)_2$-MPIBr electrolyte exhibits high-efficiency and stable 6e⁻ iodine conversion chemistry. Compared with inorganic symmetric I_2 molecules, the more easily exposed I^- center of polar C_3H_9IS combines with the oxygen in H_2O to form HIO_3, due to the lower binding energy of C_3H_9IS/H_2O (−0.81 *vs.* −0.42 eV for I_2/H_2O), which initiates I^-/IO_3^- conversion. Meanwhile, thiazole units of TZ-COFs enable strong chemical adsorption with IO_3^- species to improve redox stability with high reversibility due to reduced energy barriers (−5.1 *vs.* −3.5 eV in the AC host) and upgraded conversion kinetics (activation energy: 0.21 *vs.* 0.38 eV in AC). Owing to the halogen reaction between I^- species and Br^- halides, MPIBr can effectively activate I^+ to reduce the oxidation/reduction potential gap (0.39 V), which constitutes an important step to propel $I^-/I^0/I^+/I^{5+}$ conversion with a lower energy barrier (0.21 eV). The synergy of C_3H_9IS, TZ-COFs and MPIBr endows the Zn–I_2 batteries with ultrahigh capacity and energy density, and superior cycling stability, constituting a major advance in the design of better Zn–I_2 batteries.

Conclusion

In summary, a high conversion-efficiency and stable 6e⁻ $I^-/I_2/I^+/IO_3^-$ iodine conversion chemistry are proposed, which are enabled by the TZ-COFs/C_3H_9IS electrode in the $Zn(OTF)_2$-MPIBr electrolyte for high-performance Zn–I_2 batteries. Compared with inorganic I_2 molecules, owing to a more easily exposed I^- center to combine with the oxygen in H_2O to form HIO_3, C_3H_9IS with a polar iodine center through I^+ activation of MPIBr initiates 6e⁻ I^-/IO_3^- conversion to reduce the oxidation/reduction potential gap to show 97% iodine conversion efficiency. Meanwhile, C═N/C–S groups of thiazole units in TZ-COFs enable strong chemical adsorption with IO_3^- species to improve redox stability. Besides, thiazole units of TZ-COFs catalyze a reversible 6e⁻ conversion from I^- to IO_3^- due to reduced energy barriers and boosted conversion kinetics. Consequently, the TZ-COFs/C_3H_9IS electrode delivers a record high capacity and energy density, and long life, becoming the state-of-the-art Zn–I_2 battery electrode in comprehensive performances. This work provides a new avenue to develop efficient and stable multielectron iodine conversion chemistry for building better aqueous Zn–I_2 batteries.

Data availability

The data that support the findings of this study are available upon reasonable request from the corresponding author.

Conflicts of interest

The authors declare no conflict of interest.

Acknowledgements

This work was financially supported by the National Natural Science Foundation of China (No. 22272118, 22172111, and 22309134), the Science and Technology Commission of Shanghai Municipality, China (No. 22ZR1464100, 20ZR1460300, and 19DZ2271500), China Postdoctoral Science Foundation (2022M712402), Shanghai Rising-Star Program (23YF1449200), Zhejiang Provincial Science and Technology Project (2022C01182), and the Fundamental Research Funds for the Central Universities (2023-3-YB-07).

References

1 F. Zhu, Z. Li, Z. Wang, Y. Fu and W. Guo, *J. Am. Chem. Soc.*, 2024, **146**, 11193–11201.

2 S. Bi, H. Wang, Y. Zhang, M. Yang, Q. Li, J. Tian and Z. Niu, *Angew. Chem., Int. Ed.*, 2023, **62**, e202312982.

3 J. Hao, L. Yuan, Y. Zhu, X. Bai, C. Ye, Y. Jiao and S. Z. Qiao, *Angew. Chem., Int. Ed.*, 2023, **62**, e202310284.

4 P. Li, Y. Wang, Q. Xiong, Y. Hou, S. Yang, H. Cui, J. Zhu, X. Li, Y. Wang, R. Zhang, S. Zhang, X. Wang, X. Jin, S. Bai and C. Zhi, *Angew. Chem., Int. Ed.*, 2023, **62**, e202303292.

5 N. Li, Z. Yang, Y. Li, D. Yu, T. Pan, Y. Chen, W. Li, H. Xu, X. Guo and H. Pang, *Adv. Energy Mater.*, 2024, **14**, 2402846.

6 C. Wang, G. Gao, Y. Su, J. Xie, D. He, X. Wang, Y. Wang and Y. Wang, *Nat. Commun.*, 2024, **15**, 6234.

7 C. Wang, X. Ji, J. Liang, S. Zhao, X. Zhang, G. Qu, W. Shao, C. Li, G. Zhao, X. Xu and H. Li, *Angew. Chem., Int. Ed.*, 2024, **63**, e202403187.

8 M. Wang, Y. Meng, M. Sajid, Z. Xie, P. Tong, Z. Ma, K. Zhang, D. Shen, R. Luo, L. Song, L. Wu, X. Zheng, X. Li and W. Chen, *Angew. Chem., Int. Ed.*, 2024, **63**, e202404784.

9 J. He, Y. Mu, B. Wu, F. Wu, R. Liao, H. Li, T. Zhao and L. Zeng, *Energy Environ. Sci.*, 2024, **17**, 323–331.

10 L. Xiang, S. Yuan, F. Wang, Z. Xu, X. Li, F. Tian, L. Wu, W. Yu and Y. Mai, *J. Am. Chem. Soc.*, 2022, **144**, 15497–15508.

11 Q. Chen, S. Chen, J. Ma, S. Ding and J. Zhang, *Nano Energy*, 2023, **117**, 108897.

12 J.-L. Yang, H.-H. Liu, X.-X. Zhao, X.-Y. Zhang, K.-Y. Zhang, M.-Y. Ma, Z.-Y. Gu, J.-M. Cao and X.-L. Wu, *J. Am. Chem. Soc.*, 2024, **146**, 6628–6637.

13 S. J. Zhang, J. Hao, H. Li, P. F. Zhang, Z. W. Yin, Y. Y. Li, B. Zhang, Z. Lin and S. Z. Qiao, *Adv. Mater.*, 2022, **34**, 2201716.

14 Y. Zou, T. Liu, Q. Du, Y. Li, H. Yi, X. Zhou, Z. Li, L. Gao, L. Zhang and X. Liang, *Nat. Commun.*, 2021, **12**, 70.

15 S. Lv, T. Fang, Z. Ding, Y. Wang, H. Jiang, C. Wei, D. Zhou, X. Tang and X. Liu, *ACS Nano*, 2022, **16**, 20389–20399.

16 X. Jin, L. Song, C. Dai, Y. Xiao, Y. Han, X. Li, Y. Wang, J. Zhang, Y. Zhao, Z. Zhang, N. Chen, L. Jiang and L. Qu, *Adv. Mater.*, 2022, **34**, 2109450.

17 W. Ma, T. Liu, C. Xu, C. Lei, P. Jiang, X. He and X. Liang, *Nat. Commun.*, 2023, **14**, 5508.

18 C. Xie, C. Wang, Y. Xu, T. Li, Q. Fu and X. Li, *Nat. Energy*, 2024, **9**, 714–724.

19 X. Li, W. Xu and C. Zhi, *Nat. Rev. Chem.*, 2024, **8**, 359–375.

20 Z. Zhang, Y. Zhu, M. Yu, Y. Jiao and Y. Huang, *Nat. Commun.*, 2022, **13**, 6489.

21 T. Liu, C. Lei, H. Wang, C. Xu, W. Ma, X. He and X. Liang, *Sci. Bull.*, 2024, **69**, 1674–1685.

22 X. Li, S. Wang, D. Zhang, P. Li, Z. Chen, A. Chen, Z. Huang, G. Liang, A. L. Rogach and C. Zhi, *Adv. Mater.*, 2023, **36**, 2304557.

23 M. Liu, Q. Chen, X. Cao, D. Tan, J. Ma and J. Zhang, *J. Am. Chem. Soc.*, 2022, **144**, 21683–21691.

24 F. Wei, T. Zhang, H. Xu, Y. Peng, H. Guo, Y. Wang, S. Guan, J. Fu, C. Jing, J. Cheng and S. Liu, *Adv. Funct. Mater.*, 2024, **34**, 2310693.

25 Z. Chen, F. Wang, R. Ma, W. Jiao, D. Li, A. Du, Z. Yan, T. Yin, X. Yin, Q. Li, X. Zhang, N. Yang, Z. Zhou, Q.-H. Yang and C. Yang, *ACS Energy Lett.*, 2024, **9**, 2858–2866.

26 C. Guo, Y. Cao, Y. Gao, C. Zhi, Y. X. Wang, Y. Luo, X. J. Yang and X. Luo, *Adv. Funct. Mater.*, 2024, **34**, 2314189.

27 J. Li, X. Jing, Q. Li, S. Li, X. Gao, X. Feng and B. Wang, *Chem. Soc. Rev.*, 2020, **49**, 3565–3604.

28 L. Huang, W. Li, F. Wei, S. Ke, H. Chen, C. Jing, J. Cheng and S. Liu, *Chem*, 2024, **10**, 3103.

29 Z. Wei, Z. Huang, G. Liang, Y. Wang, S. Wang, Y. Yang, T. Hu and C. Zhi, *Nat. Commun.*, 2024, **15**, 3841.

30 Y. Wang, C. Lei, W. Guan, W. Shi, R. Shen, S. X.-A. Zhang and G. Yu, *Proc. Natl. Acad. Sci. U. S. A.*, 2024, **121**, e2401060121.

31 X. Li, M. Li, Z. Huang, G. Liang, Z. Chen, Q. Yang, Q. Huang and C. Zhi, *Energy Environ. Sci.*, 2021, **14**, 407–413.

32 P. Li, S. Yang, J. Zhu, S. Wang, Y. Hou, H. Cui, Z. Chen, R. Zhang, Z. Wu, Y. Wang, Z. Wei, X. Liu, S. Zhang, X. Li and C. Zhi, *Matter*, 2024, **7**, 1867–1878.

33 C. Dai, L. Hu, H. Chen, X. Jin, Y. Han, Y. Wang, X. Li, X. Zhang, L. Song, M. Xu, H. Cheng, Y. Zhao, Z. Zhang, F. Liu and L. Qu, *Nat. Commun.*, 2022, **13**, 1863.

34 P. Li, X. Li, Y. Guo, C. Li, Y. Hou, H. Cui, R. Zhang, Z. Huang, Y. Zhao, Q. Li, B. Dong and C. Zhi, *Adv. Energy Mater.*, 2022, **12**, 2103648.

35 S. Wang, Y. Wang, Z. Wei, J. Zhu, Z. Chen, H. Hong, Q. Xiong, D. Zhang, S. Li, S. Wang, Y. Huang and C. Zhi, *Adv. Mater.*, 2024, **36**, 2401924.

36 C. Xu, C. Lei, P. Jiang, W. Yang, W. Ma, X. He and X. Liang, *Joule*, 2024, **8**, 461–481.

37 L. Zhou, L. Zhao, X. Gao, C. Chi, Z. Qiu, Y. Song, T. Cai, P. Liu, X. Li, Z. Fan, Q. Xue, Z. Yan, Y. Cui and W. Xing, *ACS Energy Lett.*, 2023, **8**, 5152–5160.

38 R. Yang, W. Yao, L. Zhou, F. Zhang, Y. Zheng, C. S. Lee and Y. Tang, *Adv. Mater.*, 2024, **36**, 2314247.

39 K. Wang, Z. Jia, Y. Bai, X. Wang, S. E. Hodgkiss, L. Chen, S. Y. Chong, X. Wang, H. Yang, Y. Xu, F. Feng, J. W. Ward and A. I. Cooper, *J. Am. Chem. Soc.*, 2020, **142**, 11131–11138.

40 Z. Song, L. Miao, H. Duan, Y. Lv, L. Gan and M. Liu, *Angew. Chem., Int. Ed.*, 2024, **63**, e202401049.

41 Z. Song, L. Miao, Y. Lv, L. Gan and M. Liu, *Angew. Chem., Int. Ed.*, 2023, **62**, e202309446.

42 Y. Wang, X. Jin, J. Xiong, Q. Zhu, Q. Li, R. Wang, J. Li, Y. Fan, Y. Zhao and X. Sun, *Adv. Mater.*, 2024, **36**, 2404093.

43 W. Li, L. Huang, H. Zhang, Y. Wu, F. Wei, T. Zhang, J. Fu, C. Jing, J. Cheng and S. Liu, *Matter*, 2023, **6**, 2312–2323.

44 S. Wang, Z. Huang, B. Tang, X. Li, X. Zhao, Z. Chen, C. Zhi and A. L. Rogach, *Adv. Energy Mater.*, 2023, **13**, 2300922.

45 T. Liu, C. Lei, H. Wang, J. Li, P. Jiang, X. He and X. Liang, *Adv. Mater.*, 2024, **36**, 2405473.

46 J. Hu, Z. Zhang, T. Deng, F. C. Cui, X. Shi, Y. Tian and G. Zhu, *Adv. Mater.*, 2024, **36**, 2401091.

47 Z. Zhang, W. Ling, N. Ma, J. Wang, X. Chen, J. Fan, M. Yu and Y. Huang, *Adv. Funct. Mater.*, 2023, **34**, 2310294.

48 W. Li, H. Xu, H. Zhang, F. Wei, T. Zhang, Y. Wu, L. Huang, J. Fu, C. Jing, J. Cheng and S. Liu, *Energy Environ. Sci.*, 2023, **16**, 4502–4510.

49 Y. Zhang, P. Chen, Q. Wang, Q. Wang, K. Zhu, K. Ye, G. Wang, D. Cao, J. Yan and Q. Zhang, *Adv. Energy Mater.*, 2021, **11**, 2101712.

50 Q. Liu, F. Ye, K. Guan, Y. Yang, H. Dong, Y. Wu, Z. Tang and L. Hu, *Adv. Energy Mater.*, 2022, **13**, 2202908.

51 G. Li, L. Sun, S. Zhang, C. Zhang, H. Jin, K. Davey, G. Liang, S. Liu, J. Mao and Z. Guo, *Adv. Funct. Mater.*, 2023, **34**, 2301291.

52 Y. Zhang, Z. Song, L. Miao, Y. Lv, L. Gan and M. Liu, *Angew. Chem., Int. Ed.*, 2024, **63**, e202316835.

53 L.-P. Hou, X.-Q. Zhang, N. Yao, X. Chen, B.-Q. Li, P. Shi, C.-B. Jin, J.-Q. Huang and Q. Zhang, *Chem*, 2022, **8**, 1083–1098.

54 P. Jia, J. Wang, T. Zheng, C. Tao, G. Yila, L. Wang, Y. Wang and T. Liu, *Angew. Chem., Int. Ed.*, 2024, **63**, e202401055.

55 X. Zheng, Z. Song, D. Zhang, W. Du, L. Miao, Y. Lv, L. Xie, L. Gan and M. Liu, *J. Mater. Chem. A*, 2024, **12**, 15352–15360.

56 Y. Chen, L. Miao, Z. Song, H. Duan, Y. Lv, L. Gan and M. Liu, *Adv. Funct. Mater.*, 2024, **34**, 2409428.

57 Y. An, Y. Zhong, T. Sun, H. Wang, Z. Hu, H. Liu, S. Liu, Y. Kong and J. Xu, *Dalton Trans.*, 2019, **48**, 13074–13080.

58 K.-P. Shing, B. Cao, Y. Liu, H. K. Lee, M.-D. Li, D. L. Phillips, X.-Y. Chang and C.-M. Che, *J. Am. Chem. Soc.*, 2018, **140**, 7032–7042.

59 W. Zong, J. Li, C. Zhang, Y. Dai, Y. Ouyang, L. Zhang, J. Li, W. Zhang, R. Chen, H. Dong, X. Gao, J. Zhu, I. P. Parkin, P. R. Shearing, F. Lai, K. Amine, T. Liu and G. He, *J. Am. Chem. Soc.*, 2024, **146**, 21377–21388.

60 A. Y. Ya, *Russ. Chem. Rev.*, 1982, **51**, 566.

61 H. Pan, B. Li, J. Yang, W. Liu, W. Luo and B. Chen, *J. Hazard. Mater.*, 2023, **460**, 132423.

62 X. Guo, H. Xu, Y. Tang, Z. Yang, F. Dou, W. Li, Q. Li and H. Pang, *Adv. Mater.*, 2024, **36**, 2408317.

63 K. Wang, H. Li, Z. Xu, Y. Liu, M. Ge, H. Wang, H. Zhang, Y. Lu, J. Liu, Y. Zhang, Y. Tang and S. Chen, *Adv. Energy Mater.*, 2024, **14**, 2304110.

64 Y. Zhang, Z. Song, L. Miao, Y. Lv, L. Gan and M. Liu, *Adv. Funct. Mater.*, 2024, **34**, 2405710.

65 Q. Huang, L. Huang, Y. Jin, Y. Sun, Z. Song and F. Xie, *Chem. Eng. J.*, 2024, **482**, 148912.

66 Q. Huang, Y. Jin, L. Huang, Y. Cong and Z. Xu, *J. Mater. Chem. A*, 2023, **11**, 12297–12307.

67 Q. An, L. Wang, G. Zhao, L. Duan, Y. Sun, Q. Liu, Z. Mei, Y. Yang, C. Zhang and H. Guo, *Adv. Mater.*, 2023, **36**, 2305818.

68 H. Duan, K. Li, M. Xie, J.-M. Chen, H.-G. Zhou, X. Wu, G.-H. Ning, A. I. Cooper and D. Li, *J. Am. Chem. Soc.*, 2021, **143**, 19446–19453.